

# An Eigenanalysis Study of Tunable THz and Photonic Unbounded Structures Employing Finite Element Method

Volume 11, Number 5, October 2019

Konstantinos D. Paschaloudis, *Student Member, IEEE*

Constantinos L. Zekios, *Member, IEEE*

Laura Ghisa, *Member, IEEE*

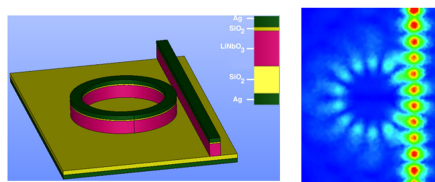
Peter C. Allilomes

Kyriakos E. Zoiros

Ammar Sharaiha

Stavros Iezekiel, *Senior Member, IEEE*






George A. Kyriacou, *Senior Member, IEEE*



LiNbO<sub>3</sub> ring resonator: geometry, E-field distribution

DOI: 10.1109/JPHOT.2019.2935805

# An Eigenanalysis Study of Tunable THz and Photonic Unbounded Structures Employing Finite Element Method

Konstantinos D. Paschaloudis <sup>1</sup>, *Student Member, IEEE*,  
Constantinos L. Zekios <sup>2</sup>, *Member, IEEE*,  
Laura Ghisa,<sup>3</sup> *Member, IEEE*, Peter C. Allilomes,<sup>1</sup>  
Kyriakos E. Zoiros,<sup>1</sup> Ammar Sharaiha <sup>3</sup>,  
Stavros Iezekiel <sup>4</sup>, *Senior Member, IEEE*,  
and George A. Kyriacou <sup>1</sup>, *Senior Member, IEEE*

<sup>1</sup>Department of Electrical and Computer Engineering, Democritus University of Thrace,  
Xanthi 671 00, Greece

<sup>2</sup>Florida International University, Miami, FL 33199 USA

<sup>3</sup>Lab-STICC (UMR CNRS 6285), École National d'Ingénieurs de Brest, Brest 29280, France

<sup>4</sup>Department of Electrical and Computer Engineering, University of Cyprus, Nicosia 1678,  
Cyprus

DOI:10.1109/JPHOT.2019.2935805

This work is licensed under a Creative Commons Attribution 4.0 License. For more information, see  
<https://creativecommons.org/licenses/by/4.0/>

Manuscript received April 3, 2019; accepted August 12, 2019. Date of publication August 19, 2019; date of current version September 6, 2019. Corresponding author: George A. Kyriacou (e-mail: gkyriac@ee.duth.gr).

**Abstract:** This work aims at the establishment of a rigorous full-wave eigenmode analysis technique based on a finite element scheme for the study of terahertz (THz) or photonic/optical unbounded structures. This numerical tool follows the last decades' trend to migrate the technological knowledge from microwave to THz and photonic regimes. The performed eigenanalysis offers an insightful view of the studied structures, revealing their characteristics. For the truncation of the infinite solution domain, the first kind absorbing boundary conditions are employed, while the involved spurious modes are eliminated with the incorporation of a tree-cotree splitting formulation. The study focuses on tunable microring resonators supporting leaky-radiating wave propagation and bounded-resonating whispering gallery modes. Tunability is achieved by integrating an electro-optical layer and in turn through the enforcement of an external applied DC electric field. An innovative approach constitutes the numerical determination of the altered dielectric permittivity as a piecewise constant distribution rather than a constant mean value.

**Index Terms:** Microwave photonics, microring resonator, finite element method, spurious modes, tree-cotree, unbounded structures, Lithium Niobate.

## 1. Introduction

Microwave Photonics offers exciting prospects for the realization of future wireless systems for 5G and beyond, operating up to mm-wave and THz carrier frequencies. The air interfaces of the RF front-ends in such systems will have to operate in an agile manner to some tens of GHz for cognitive radio applications. In this respect, the large bandwidth of optical fiber and the ability to modulate light to several tens of GHz and then detect it, as well as the capability of generating THz signals photonically, is of great interest. Moreover, the photonic approach offers tunability over a high frequency range, and the implementation of controllable true-time-delay (TTD) devices with low

distortion will be invaluable [1]–[4]. Furthermore, as integrated circuits approach their speed limits, increased use of photonics (including photonic integrated circuits) will need to be considered, [5].

Over the last decade, there has been a growing trend to migrate the techniques used for the electromagnetic study of microwave geometries to the THz and photonic domain, [6]–[11]. Even though Maxwell's equations remain valid at these higher frequencies [7], [12], the extension of microwave simulators to the THz and photonic domains is not straightforward. The main difficulty stems from the operating frequency being three to five orders of magnitude higher than those in microwave structures, in conjunction with the domain discretization in a fraction of the wavelength (at least  $\lambda/10$ , where  $\lambda$  is in the sub-micrometer range). Thus, the resulting structures are electrically huge, rendering their study computationally demanding. The situation is even worse in the case of an eigenanalysis, where a larger solution domain leads to more spurious solutions (both DC and imaginary), preventing convergence to a solution. In order to overcome them, a rigorous eigenanalysis electromagnetic simulator based on a finite element scheme is described in this paper, aiming to reveal the electromagnetic characteristics and provide an insightful view of the studied structures. The case of microring based resonators are thoroughly analyzed.

Note that due to high metal losses in the THz and optical frequencies, the imaginary spurious modes are expected to become complex. For the suppression of these non-physical solutions a tree-cotree technique is employed, which ensures a divergent free formulation through the enforcement of the appropriate constrained equations in the solution domain, [9], [13].

A major issue involved in the extension to THz-Photonic frequencies is the modeling of the metallic parts of the studied geometries, because at these frequencies, metals exhibit a highly lossy and dispersive nature, [7], [8], [12], [13]. Hence they cannot be treated as perfect electric conductors, but rather as a highly lossy dielectric with negative real part for the dielectric permittivity. The Lorentz-Drude model is employed for the determination of this permittivity, which depends on both the type of metal and the operating frequency, [14]–[16]. This behavior of metals at high frequencies affects also their skin depth, which tends to be comparable to the structures' thickness, [7], [16]–[18]. Thus, the metallic parts are discretized as volume finite elements with a complex dielectric constant just as a dielectric layer, in contrast to the microwave regime where they are considered as PEC (perfect electric conductor) surfaces modeled through the enforcement of boundary conditions.

Concerning now the photonic structure development, this faces serious limitations related primarily to the fabrication procedure. In particular, the design of optical microcavities demands optical waveguides that are able to better confine the light. However, realizing such a wave-guide is difficult due to the requirement of better refractive index contrast. Hence, materials with extremely low refractive index, even lower than Silica ( $n_{SiO_2} = 1.45$ ), are demanded, which are not available, [19]. This lack of the appropriate materials in combination with the absence of simple design rules for THz and photonic structures make the numerical analysis of these structures crucial before their fabrication, [20]. There are already published works that efficiently employ the Method of Moments (MoM) for the numerical study of plasmonic structures for nanoantenna applications, [12], [20]. However, MoM usually results in matrices with poor condition numbers, giving rise to numerical instability of the studied problem, [21]. Furthermore, the existence of Greens functions in the formulation of MoM algorithms not only requires much greater analytical effort, but it also makes the study of geometrically complicated structures impossible.

Hence, for the study of complex nanotopologies, a numerical procedure based on differential equations techniques is inevitable. In the current work, an eigenanalysis tool based on finite element method (FEM) is employed in order to physically understand the electromagnetic properties of the examined nanostructures. A finite element technique is preferred herein instead of a finite difference in time domain (FDTD) approach, not only due to the involved staircase effect, but also due to the robustness that FEM exhibits. Accounting for absorbing boundary conditions (ABCs) and the material losses, either dielectric or metallic, yields a complex non-linear generalized eigenvalue problem. The corresponding characteristic polynomial is formulated as a quadrature problem, which is linearized either by an eigenvector transformation or by a companion linearization, [13].

The current work also studies the electronic reconfiguration of THz and photonic topologies, through the utilization of the linear electro-optical phenomenon (Pockel's effect), [22]. This is

motivated by the fact that electronically steerable phased arrays will play a key role in 5G communication systems. Tunable THz or photonic structures, such as microring resonators, could fulfill this role, introducing the appropriate true-time-delay (TTD), thereby avoiding the beam-squint in ultra-wideband phased arrays.

Thermo-optical tuning dominates in the domain of microring resonators, [23], instead of electro-optical tuning, due to the great advances in silicon-on-insulator (SOI) technology. However, tuning the resonant frequencies of these devices through thermal means is neither efficient nor accurate, especially in integrated circuit cases. Therefore, the current work studies electro-optical tuning of lithium niobate ( $LiNbO_3$ ) devices [24]–[28] through the application of an externally applied DC voltage. The optical permittivity and the related index of refraction both depend generally on the intensity of the electric field in a complicated non-linear form, but it can be approximated by the linear electro-optic effect for the relatively low intensities considered herein. For a locally homogeneous electric field, convenient closed form expressions for the resulting tensor optical permittivity are given in [29]. The usual approach followed until now is to estimate an average value of the electrostatic field within the  $LiNbO_3$  and calculate the corresponding permittivity tensor, assumed constant-homogeneous throughout this media, [30]. However, in practice the electrostatic potential and the related electric field generated by electrodes are not homogeneous. Thus, within the present effort, the electrostatic problem is solved numerically by employing FEM. In turn, the average electrostatic field is calculated at each finite element barycenter and the expressions of [29] are utilized to yield a piecewise homogeneous optical permittivity tensor distribution. Thus, a realistic inhomogeneous numerical model is adopted in this work to describe tunable electro-optical media.

Regarding the application, the current work focuses on the study of tunable ring resonators, which are established as traveling wave-integrated optical resonators, [19], [31]–[35]. In general, optical microcavities are utilized extensively in the design of various optical applications, such as modulators, all-optical nonlinear switching, all-optical signal processing, slow-light structures or optical buffers and wavelength division-multiplexed (WDM) optical filters, [36]–[42]. Hence, this paper carries out a thorough analysis of the performance of an all-pass tunable phase or tunable time delay filtering structure comprised of a ring resonator side-coupled to a bus waveguide.

The paper is organized as follows. In Section 2 the eigenvalue problem with its appropriate finite-element discretization, treatment of metal in the photonic regime, a linearization technique for the solution of polynomial eigenvalue problem and the  $LiNbO_3$  dielectric permittivity changes due to applied DC voltage are presented. Section 3 presents the numerical results and is divided into three part. The first part studies the convergence of the proposed methodology, and presents a validation procedure; the second part is dedicated to metal characterization in photonic frequencies, where different models and measurements are compared; and the last part presents the results of the ring resonator filtering structures. Finally, a brief summary of the key attributes of the current work is provided in Section 4.

## 2. Formulation

An indicative geometry as shown in Fig. 1 is used to demonstrate the proposed methodology. It contains a microring resonator which is side-coupled with a hybrid plasmonic waveguide (HPW), [43]–[44]. It consists of a silica layer between a lithium niobate layer and a silver superstrate (acting as the active electrode) which all reside on a silica substrate. Underneath the silica substrate, another silver ring lies acts as the ground electrode. Values of the geometrical parameters are listed in the caption of Fig. 1. Although a specific geometry is assumed, a general formulation for the proposed eigenvalue problem follows.

### 2.1 Eigenvalue Problem

The whole structure is enclosed by a fictitious parallelepiped, where the Absorbing Boundary Conditions (ABCs) are enforced, implementing the truncation of the unbounded solution domain. The vector wave equation for a source free structure, loaded with tensor permittivity ( $\vec{\epsilon}_r$ ) and tensor

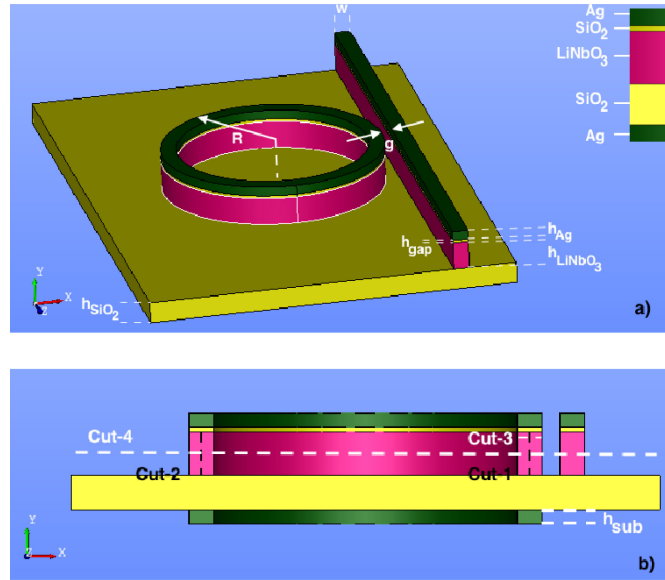


Fig. 1. a) Tunable microring resonator phase filtering geometry with geometrical parameters  $R = 1.2 \mu\text{m}$ ,  $g = 120 \text{ nm}$ ,  $w = 170 \text{ nm}$ ,  $h_{\text{Ag}} = 100 \text{ nm}$ ,  $h_{\text{gap}} = 30 \text{ nm}$ ,  $h_{\text{LiNbO}_3} = 300 \text{ nm}$ ,  $h_{\text{SiO}_2} = 230 \text{ nm}$ ,  $h_{\text{sub}} = 100 \text{ nm}$  and b) z-cut view with some mentioned cuts.

permeability ( $\bar{\bar{\mu}}_r$ ) anisotropic materials, reads, [45]:

$$\bar{\nabla} \times \bar{\bar{\mu}}_r^{-1} \cdot \bar{\nabla} \times \bar{E} - k_0^2 \bar{\bar{\epsilon}}_r \bar{E} + jk_0 Z_0 \bar{\bar{\sigma}} \bar{E} = 0 \quad (1)$$

where  $Z_0 = 120\pi \Omega$  stands for the free space impedance. The imaginary parts of ( $\bar{\bar{\epsilon}}_r$ ) and ( $\bar{\bar{\mu}}_r$ ) represent the losses due to electric and magnetic polarization respectively, while the Joule losses are accounted for by a tensor conductivity ( $\bar{\bar{\sigma}}$ ).

Concerning the metals in the THz and photonic regime, they are modeled as lossy dielectrics with a related dielectric constant and conductivity rather than perfect electric conductors. For sake of convenience, a complex permittivity accounting for both displacement current and conductivity current losses will be introduced as, [9]:

$$\bar{\bar{\epsilon}}^* = \bar{\bar{\epsilon}} - j \frac{\bar{\bar{\sigma}}}{\omega} = \epsilon_0 \bar{\bar{\epsilon}}_r^*, \quad \bar{\bar{\epsilon}}_r^* = \bar{\bar{\epsilon}}_r - j \frac{\bar{\bar{\sigma}}}{\omega \epsilon_0} \quad (2)$$

Incorporation of these types of losses retains the same form of eigenvalue problem as in the lossless case and the only difference is observed for the resulting eigenvalue  $k_0$ , which becomes complex. For the determination of this complex permittivity as a function of frequency, the Lorentz-Drude model is incorporated, [14]–[16]:

$$\epsilon_r(\omega) = \epsilon_r^{(f)}(\omega) + \epsilon_r^{(b)}(\omega) \quad (3a)$$

$$\epsilon_r^{(f)}(\omega) = 1 - \left( \frac{f_0 \omega_p^2}{\omega(\omega - j\Gamma_0)} \right) \quad (3b)$$

$$\epsilon_r^{(b)}(\omega) = \sum_{j=1}^k \frac{f_j \omega_p^2}{(\omega_j^2 - \omega^2) + j\omega \Gamma_0} \quad (3c)$$

where the superscript (f) refers to the free electron effects (intraband effects), the superscript (b) to the bound-electron effects (interband effects),  $f_0$  to the oscillation strength,  $\omega_p$  to the plasma frequency,  $\Gamma_0$  to the damping factor ( $\tau = 1/\Gamma_0$ ,  $\tau$ : relaxation time), while k refers to the number of

oscillators with frequency  $\omega_j$ , strength  $f_j$ , and lifetime  $1/\Gamma_j$ . The Lorentz- Drude model constitutes a good fit especially for dispersive silver in the spectral range of energies below 2 eV, where there is a good agreement between the analytical and experimental values from [46].

Applying the standard Galerkin procedure to (1) the following weak formulation can be derived, [45]:

$$\begin{aligned} & \iiint_V (\nabla \times \bar{T}) \cdot \bar{\mu}_r^{-1} (\nabla \times \bar{E}) d\Omega - k_0^2 \iiint_V \bar{T} \cdot (\bar{\epsilon}_r \bar{E}) d\Omega \\ & + jk_0 Z_0 \iiint_V \bar{T} \cdot (\bar{\sigma} \bar{E}) d\Omega - jk_0 Z_0 \iint_S \bar{T} \cdot (\hat{n} \times \bar{H}) dS = 0 \end{aligned} \quad (4)$$

where  $k_0 = \omega/c$  is the free space wavenumber and  $T$  is the vector weighting function. Note that a complex eigen-frequency will be now obtained due to losses, where its imaginary part defines the quality factor as  $Q = \text{Re}(k_0)/(2\text{Im}(k_0))$ . It is evident from Fig. 1 that the studied geometry refers to an unbounded structure, so the truncation of the domain is required. This is realized applying the ABCs of 1st kind, [47]. Thus, neglecting the contribution of the third integral that represents the conductivity caused by migrating charge carriers in a lossy material, (4) takes the form:

$$\iiint_V (\nabla \times \bar{T}) \cdot \bar{\mu}_r^{-1} (\nabla \times \bar{E}) d\Omega - k_0^2 \iiint_V \bar{T} \cdot (\bar{\epsilon}_r \bar{E}) d\Omega + jk_0 \iint_S (\hat{n} \times \bar{T}) \cdot (\hat{n} \times \bar{E}) dS = 0 \quad (5)$$

The presence of the bus waveguide in the studied domain requires a special analysis for its input and output parts. A similar approach has already been employed by Ketzaki *et al.*, [23], who studied thermo-optically tunable structures. Explicitly, ordinary 1st kind ABCs are imposed on the whole truncation surface apart from the waveguides input and output ports. Over these surfaces an appropriate termination is imposed. Actually, these wave terminations are located slightly inside the ABCs truncating box. In this way, ABCs can be applied over the whole truncating box without any port exception. Therefore, a 2D eigenanalysis is applied at the input and output port in order to attain the field distribution of the dominant mode, [48]–[49]. We retain only the dominant mode of the field, since the higher order modes are evanescent at the terminal planes. However, this fundamental mode refers to a hybrid one, since the studied structure employs a hybrid plasmonic waveguide (HPW). The modified ABCs should account for the coordinate-dependent wave impedance, [50]. The resulting term for the input/output-port termination conditions is similar to that of [23] and reads:

$$\hat{n} \times \nabla \times \bar{E} + \bar{\gamma} \hat{n} \times \hat{n} \times \bar{E} = 0 \quad (6a)$$

$$\text{where } \bar{\gamma} = \frac{j\omega\mu_0}{Z_w^{TE}(x, y)} \hat{x}\hat{x} + \frac{j\omega\mu_0}{Z_w^{TM}(x, y)} \hat{y}\hat{y} \quad (6b)$$

$$Z_w^{TE}(x, y) = \frac{E_x(x, y)}{H_y(x, y)} \quad (6c)$$

$$Z_w^{TM}(x, y) = -\frac{E_y(x, y)}{H_x(x, y)} \quad (6d)$$

Here  $Z_w^{TE}(x, y)$  and  $Z_w^{TM}(x, y)$  refer to the wave impedances of the TE and TM mode respectively. Overall, the final formulation of the eigenvalue problem can be expressed in matrix form as:

$$[S][e] - k_0^2[M][e] + jk_0[R][e] = 0 \quad (7)$$

$$[S] = \iiint_V (\nabla \times \bar{T}) \cdot \bar{\mu}_r^{-1} (\nabla \times \bar{E}) d\Omega \quad (8)$$

$$[M] = \iiint_V \bar{T} \cdot (\bar{\epsilon}_r \bar{E}) d\Omega \quad (9)$$

$$[R] = \iint_{S_{\text{outer}}} \bar{T} \cdot (\hat{n} \times \bar{H}) dS + Z_0 Z'_w \iint_{S_{\text{ports}}} \bar{T} \cdot (\hat{n} \times \bar{H}) dS \quad (10)$$

where  $Z'_w$  stands for:

$$Z'_w = \frac{1}{Z_w^{TE}(x, y)} \hat{x}\hat{x} + \frac{1}{Z_w^{TM}(x, y)} \hat{y}\hat{y} \quad (11)$$

Equation (7) depicts evidently the nonlinear, but polynomial, form of the resulting generalized eigenvalue problem. This nonlinearity is the result of the incorporation of ABCs and the frequency dependent Drude model permittivity of the metallic parts at THz and optical frequencies. Therefore, the use of a non-linear eigensolver or the incorporation of linearization technique is demanded for the solution of the eigenproblem (7). In this paper, in order to overcome the non-linearity arising from the frequency dispersive dielectric permittivity, which influences matrix [M] directly, an initial estimation for the eigenvalue  $k_0^0$  of the expected eigenmode is performed, [51]. The main idea is to handle the non-linearity caused by the ABCs employing a linearization technique, just as in our previous work, [9], [53], assuming a given complex dielectric constant for the metallic structures. This value is initially selected as the one at the central frequency of the examined band. Having this estimation, the dielectric permittivity of the metallic parts is determined using the Lorentz-Drude model and the matrix [M] can be constructed. Then, the incorporation of the linearization technique, which follows in the next paragraph, is performed in order to numerically solve the resulting eigenproblem. In turn, the solution of the eigenproblem yields a vector-group of complex resonant eigenfrequencies represented by  $k_0^1$ , which is used to reconstruct matrix [M], resolve the eigenproblem and yield further estimates  $k_0^2, k_0^3$ , etc. This procedure is terminated when two consecutive estimations of the eigenvalue is changed less than a prescribed error tolerance.

Trying to directly solve the above eigenproblem (7)–(10), the appearance of non-physical, but mathematically valid, eigen-solutions, either DC or imaginary, occurs. As explicitly explained in [9], [53], the weak form of (5) or its discretized form (7) to (11) exhibits these solutions due to the inability of this equation to directly enforce the required zero divergence condition. The same situation stands for all the eigenproblems resulting from the vector wave equation. Some of these spurious solutions could be easily identified and discarded at the post-processing level. Recall that in the microwave regime, where metals are assumed as perfect electric conductors (PEC), it is known that the number of spurious modes is equal to the number of free nodes (nodes not belonging to a PEC area), e.g. [9], [13], [53]. In the present case, where metals are modeled as lossy dielectrics, there are not any PEC-nodes, hence the total number of nodes are free nodes. Namely, they are free to accumulate fictitious charges not obeying zero divergence law or from a different point of view to support spurious modes. In this highly lossy case, all spurious modes are expected to exhibit complex or zero eigenvalues, instead of imaginary or zero ones occurred in the lossless case. In addition, it was shown in [9] and in more detail in Zekios' doctoral thesis [53], that in the case where the original eigenproblem (7)–(10) is directly solved, the algorithm fails to properly converge, involving errors higher than 0.3 up to 0.6, where the error is defined by the norm of the system in (7). In contrast, when the eigenproblem is constrained by the divergence free condition, the error is dramatically reduced to  $10^{-15}$ , apart from the complete elimination of the spurious modes (accompanied by a substantial algorithm speedup). The implementation therefore of the tree-cotree technique, as described in [53] and precisely as extended in the case of non-linear problems with unbounded domains in [9], is utilized for the removal of DC, imaginary and possibly complex spurious solutions.

## 2.2 Linearization Technique

The formulation of the eigenvalue problem (7) results in a nonlinear form. As a result, a linearization technique should be applied to its numerical solution. Setting  $k_0 = \lambda$ , the formulation in (7) is transformed into a single standard quadrature problem with a characteristic polynomial:

$$P(\lambda) = -\lambda^2 M + \lambda R + S = 0 \quad (12)$$

which can be written using a companion linearization form as:

$$\left( \lambda \begin{bmatrix} R & -M \\ -I & 0 \end{bmatrix} + \begin{bmatrix} S & 0 \\ 0 & I \end{bmatrix} \right) \begin{bmatrix} e \\ u \end{bmatrix} = \begin{bmatrix} 0 \\ 0 \end{bmatrix} \quad (13)$$

where  $I$  refers to the identity matrix,  $e$  is the seeding vector and  $k_0[e] = [u]$  represents an eigenvector transformation. The resulting generalized eigenvalue problem is solved for the complex wavenumber  $k_0 = \omega/c$ , where  $\omega = \omega_r + j\omega_i$ , utilizing a shift and invert Arnoldi method. The resonant frequency of the structure is derived using the real part of the wavenumber as  $f_{res} = \omega_r/2\pi$ , while the imaginary part is useful for the determination of the corresponding quality factor as  $Q_{res} = \omega_r/(2\omega_i)$ .

### 2.3 Tunability of $LiNbO_3$ Dielectric Permittivity

As mentioned in the introduction, electronic reconfiguration of the studied structures is implemented by varying the dielectric permittivity of  $LiNbO_3$ . These changes result from an externally applied static electric field exploiting the linear electro-optic phenomenon exhibited by  $LiNbO_3$ .

In calculating the electric field distribution in a domain without the presence of high frequency sources, it is important to handle an equation that properly defines the electric field at DC. This is the generalized Laplace equation rather than the ordinary one, as it allows for heterogeneous material loading, [54]. Although one would expect to solve the generalized Poisson equation in the presence of the DC-biasing source, it is more convenient to solve the source free generalized Laplace equation where the DC-voltage (or current) source is enforced through appropriate boundary conditions. Hence in the case of the structure of Fig. 1, where heterogeneous conductivity is present, the governing law takes the form:

$$\bar{\nabla} \cdot \sigma(x, y, z) \bar{\nabla} V(x, y, z) = 0 \quad (14)$$

where  $\sigma(x, y, z)$  is the coordinate-dependent electrical conductivity and  $V$  the electrostatic potential. Although, (14) could be solved analytically in the cases of simplified structures, a numerical approach using FEM is needed here due to the geometrical complexity and the presence of inhomogeneous materials. After the numerical determination of the DC electric potential distribution, the static electric field can be calculated.

Based on the value of the estimated electric field at each finite element barycenter, the closed form expression introduced in [29], is used for the determination of the altered dielectric permittivity of  $LiNbO_3$ . Following this approach, the resulting dielectric permittivity is considered as a piecewise homogeneous optical permittivity tensor distribution. This is a rather innovative approach compared to the typical approach, where a constant homogeneous permittivity tensor throughout the  $LiNbO_3$  is considered, whereas our approach uses a realistic inhomogeneous numerical model. Subsequently, this optical permittivity tensor distribution is utilized in the solution of the THz or photonic eigenvalue problem (7).

## 3. Numerical Results

In this section we initially focus on the convergence and the validation of the proposed methodology, before examining different models and measurements for metal characterization at THz and photonic frequencies. Finally, the characteristics of ring resonator filtering structures are studied. Both the geometry design and the mesh initialization are performed using the free open-source software SALOME, [55]. Concerning the proposed FEM technique, an in house code is developed and incorporated in the open-source platform FEniCS, [56].

### 3.1 Convergence Procedure

In order to validate the proposed methodology and check the algorithms convergence, the geometry of Fig. 2 studied by Ketzaki *et al.* [23], is investigated. It consists of an uncoupled ring resonator made of two silica ( $n_{SiO_2} = 1.45$ ), one silicon ( $n_{Si} = 3.48$ ) and one silver layer ( $n_{Ag} = 0.14 - j11.4$ ),



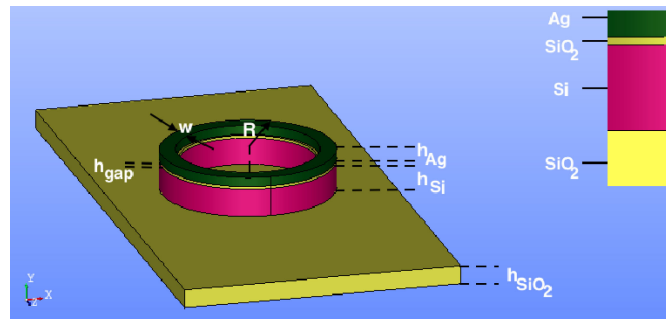


Fig. 2. Uncoupled microring resonator geometry with geometrical parameters  $R = 0.945 \mu\text{m}$ ,  $w = 170 \text{ nm}$ ,  $h_{\text{Ag}} = 100 \text{ nm}$ ,  $h_{\text{gap}} = 30 \text{ nm}$ ,  $h_{\text{Si}} = 300 \text{ nm}$ ,  $h_{\text{SiO}_2} = 230 \text{ nm}$ . The material properties, as given in [23], are:  $n_{\text{Si}} = 3.48$ ,  $n_{\text{SiO}_2} = 1.45$ ,  $n_{\text{Ag}} = 0.14 - j11.4$ .

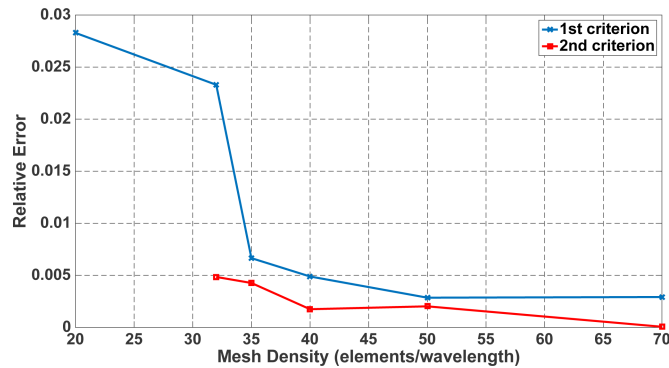


Fig. 3. Relative error versus mesh density for the eigenmode around 1550 nm.

with the geometrical parameters listed in the caption of Fig. 2. An initial finite element mesh of tetrahedrals with a discretization of 20 elements per wavelength ( $\lambda$ ) is created. A further increase in mesh density over the whole structure renders the eigenproblem electrically huge, but the strong field variations (high gradients) are expected only within the ring and on its neighborhood. Hence, a selective mesh densification is employed. For this purpose, the ring and its neighborhood are enclosed within a pseudo ring object, where the mesh density is increased up to  $\lambda/32$ . Two error criteria are introduced to check the algorithms convergence. For the first criterion, the solution of [23] is considered as a reference to define a relative error. For the second criterion, the relative error between successive eigenvectors values is defined. The two relative errors versus the number of elements per wavelength within the pseudo-object are illustrated in Fig. 3. It is concluded that a mesh density of  $\lambda/50$  within the pseudo-object and  $\lambda/20$  over the remaining structure offers an acceptable accuracy.

### 3.2 Suppression of Spurious Modes and Validation Test

Ten representative high order eigenvalues for the structure of Fig. 2 are listed in Table 1, where the enforcement of the constraint equations clearly eliminates the occurrence of spurious modes. By contrast, the unconstrained case exhibits several spurious eigenvalues, some of them being zero eigenvalues (1 to 3), some others are complex (4 to 5), while others are imaginary (6 to 8). To ensure that the constraint has been well incorporated, the divergence of the eigenvectors is computed and tabulated in Table 1, as an error measurement  $\text{err}(e) = ||G^T M e + G^T R e||$ . The divergence must be applied to all matrices (mass [M] and resistance [R]) and not only on the mass matrix as in the linear case [53], because here the constraint is enforced for the whole system. Observing the resulting

TABLE 1  
Higher Order Eigenvalues for the Microring Structure of Fig. 2 Computed With and Without Constrained Equations

Mode No	Constrained		Unconstrained	
	$k_0 \left(1 + \frac{j}{2Q}\right)$	err(e)	$k_0 \left(1 + \frac{j}{2Q}\right)$	err(e)
1	3.5795+j0.31237	4.93e-14	4.28e-06+j2.5e-06	0.26
2	3.5809+j0.31237	6.14e-14	5.16e-07+j9.54e-08	0.28
3	3.6172+j0.01215	1.25e-13	8.28e-08+j6.57e-07	0.36
4	3.6176+j0.01213	5.97e-14	0.01+j0.634	0.64
5	4.0498+j0.00661	1.17e-13	0.99+j0.123	0.78
6	4.0501+j0.00662	8.26e-14	5.73e-12+j97.928	0.03
7	4.1537+j0.33261	2.15e-13	5.56e-13+j98.043	0.01
8	4.1555+j0.33358	14e-13	-9.73e-15+j98.319	0.01
9	4.4473+j0.00375	2.67e-13	4.4473+j0.00375	0.001
10	4.4474+j0.00375	2.7e-13	4.4474+j0.00375	0.001

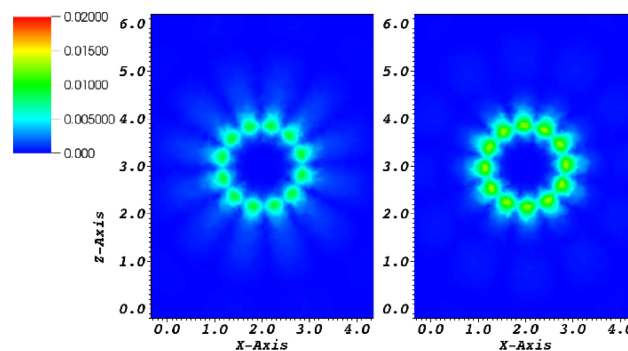


Fig. 4. Electric field distributions of the pairs of modes #1, 2 of Table I both with azimuthal mode index equal to 6.

TABLE 2  
Validation of Three Representative Eigenvalues for the Microring Structure of Fig. 2

Mode No	Azimuthal mode index (AI)	Computed		Ref. [23]	
		Resonant wavelength [nm]	Q	Resonant wavelength [nm]	Q
3	6	1737	148	1743	175
5	7	1551	306	1556	355
9	8	1413	593	1418	675

eigenvalues in the constrained case, these appear in pairs, where their real part slightly differs from one another. At first sight, this can be interpreted as an occurrence of spurious solutions. However, the corresponding eigenvectors are different, as depicted in Fig. 4 for the modes #1, 2, which indicates the existence of mode degeneration. One possibility of mode degeneration is the occurrence of right (RHCP) and left (LHCP) hand circularly polarized modes, which even though they have the same eigenvalue, the field is temporally rotated in a different sense. This assumption will be investigated in future work. Some of the resulting eigenvalues of the constrained case are further tested against those of [23] as presented in Table 2, where it is evident that they are in good agreement. The minor deviations in the quality factors result probably from the consideration of higher state of losses and energy leakage in our methodology.

### 3.3 Metal Characterization in Photonic Regime

As mentioned in the introduction, the treatment of metallic regions at THz and photonic frequencies constitutes a challenging issue, not only due to their highly lossy and dispersive nature, but also due to their frequency dependent behavior. This challenge has been addressed either with the use of

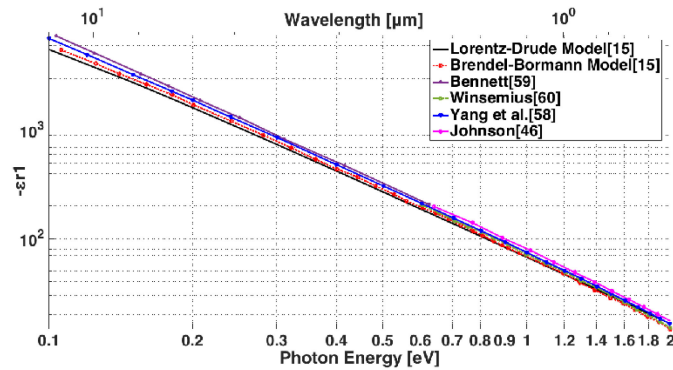


Fig. 5. Negative real part of silver ( $A_g$ ) dielectric function  $\epsilon_{r1}$  versus the photon energy derived from various models and experimental results.

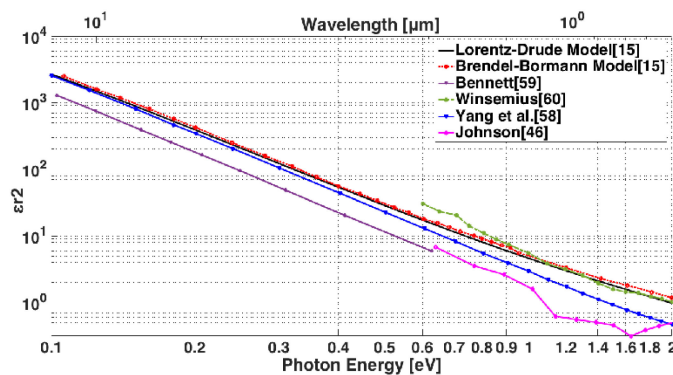


Fig. 6. Imaginary part of silver ( $A_g$ ) dielectric function  $\epsilon_{r2}$  versus the photon energy derived from various models and experimental results.

parameterized models for the determination of the dielectric function of metals ( $\epsilon_r = \epsilon_{r1} - j\epsilon_{r2}$ ), like the Lorentz-Drude and the Brendel-Bormann models, or by conducting measurements, [15], [46], [57]–[60]. The current work employs the Lorentz-Drude model (equations 3, 3a, 3b) as presented in [15], which is compared in Fig. 5 and Fig. 6 with other models [15] and experimental results [46], [57]–[60] for the case of silver. The results of Lorentz-Drude model exhibit in general a good fit with the other results in the area of interest (800–1600 nm), particularly for the real part. Concerning the imaginary part, there are some relative variations among published values, as observed in Fig. 6. However, these deviation from Lorentz-Drude model are minor for most results, except those of Bennett and Johnson, [46], [59]. However, Bennett does not cover the area of our interest, and Johnsons results in the energy area of 0.6–2.0 eV exhibit a significant uncertainty, as also stated by Yang *et al.* [58]. For the characterization of silver in the geometry of Fig. 2, the authors of [23] use the data of [46]. In particular, the utilized refractive index value for silver ( $n_{Ag} = 0.14 - j11.4$ ) corresponds to a reference wavelength around 1550 nm and is used for the entire simulation procedure. For the validation phase only, the same value is used in our algorithm with the results presented in Table 1 and Table 2. However, Fig. 5 and Fig. 6 show that the Johnsons values for the dielectric function of silver, [46], have significant deviations from other published measurements and models.

Using the Lorentz-Drude model [15] for the determination of dielectric constant of silver at 1550 nm, the resulting refractive index is  $n_{Ag} = 0.39 - j10.29$  (or  $\epsilon_r^{Ag} = -105.7 - j8.02$ ) instead of  $n_{Ag} = 0.14 - j11.4$  (or  $\epsilon_r^{Ag} = -129.8 - j3.19$ ) as used in [23] and here to extract the results of Table 2. The resulting resonant wavelengths and quality factors are listed in Table 3 and compared with the previously computed ones. Significant shifts of the resonant wavelengths are observed as a result

TABLE 3

Cross Examination of Three Representative Eigenvalues for the Microring Structure of Fig. 2 Using Different Characterization Approaches for Silver

Mode No	Azimuthal mode index (Al)	Johnson's Data, [46]		Lorentz-Drude Model's Data (fixed values at 1550 [nm]), [15]	
		Resonant wavelength [nm]	Q	Resonant wavelength [nm]	Q
3	6	1737	148	1754	79
5	7	1551	306	1562	137
9	8	1413	593	1419	226

TABLE 4

Cross Examination of Three Representative Eigenvalues for the Microring Structure of Fig. 2 Using Different Characterization Approaches for Silver

Mode No	Azimuthal mode index (Al)	Lorentz-Drude Model's Data (fixed values at 1550 [nm]), [15]		Lorentz-Drude Model's Data, [15]	
		Resonant wavelength [nm]	Q	Resonant wavelength [nm]	Q
3	6	1754	79	1735	88
5	7	1562	137	1561	138
9	8	1419	226	1425	201

of different value for the dielectric constant silver. Furthermore, the large reductions of the quality factors are due to the higher imaginary part of dielectric function, which implies a shorter relaxation time  $\tau$ , and correspondingly larger damping factor  $\Gamma_0$ .

Nevertheless, the use of the same mean value for the dielectric constant of silver for the whole frequency spectrum degrades the resulting eigenvalues, since this is considered as frequency independent in the area of interest, which Fig. 5 and Fig. 6 show to be a wrong assumption. Table 4 presents the calculated resonant wavelengths and the corresponding quality factors utilizing the dielectric constants from Lorentz-Drude model. Namely, the left column of Table 4 refers to a fixed silver dielectric constant evaluated at 1550 nm, and the right column the non-linear eigenproblem where the silver dielectric constant is a function of wavelength. The dielectric constant data for both cases are extracted from [15]. It is observed that the results for mode #5 resonating at 1550 nm remain almost unchanged, since the metal complex dielectric constant used before (e.g. Table 2) was for that wavelength.

The results listed in Table 3 and Table 4 prove the importance of the correct characterization of metals at THz and photonic frequencies. An inaccurate consideration of their dielectric constant can corrupt the structure development and lead to wrong results. For example, in the design of microring resonator filtering structures, an erroneous result provokes the shift of the resonant wavelength, which renders the filter useless.

### 3.4 Ring Resonator Filtering Structure

The characteristics of ring resonator filtering structures are examined in a two-step simulation procedure. First, the case of a single uncoupled ring resonator is considered, in order to obtain the supporting whispering gallery modes (WGMs). In the second part, the case of the same ring resonator side-coupled with a bus hybrid plasmonic waveguide (HPW) is employed. This structure serves actually as an all-pass filter, the electronic reconfiguration of which is examined below.

**3.4.1 Analysis of the Uncoupled Ring Resonator:** The study of the uncoupled ring resonator case (ignoring the existence of a waveguide) offers an insightful view of the possible natural modes of the resonator. It also reveals characteristics such as their resonant frequencies and the corresponding quality factors, as well as the modal field distributions. The studied geometry is depicted in Fig. 1 and its geometrical characteristics are presented in paragraph 2. Concerning now its material characteristics, the refractive index of silica is  $n_{SiO_2} = 1.45$ , of  $LiNbO_3$  are  $n_{0,LiNbO_3} = 2.2113$

TABLE 5

Three Representative Eigenvalues for the Uncoupled Case of Microring Structure of Fig. 1 Compared With the Corresponding of Fig. 2

Azimuthal mode index (Al)	Silicon case (Fig. 2)		$LiNbO_3$ case (Fig. 1)	
	Resonant wavelength [nm]	Q	Resonant wavelength [nm]	Q
6	1735	88	1769	23
7	1561	138	1540	30
8	1425	201	1367	38

TABLE 6

Higher Order Eigenvalues for the Uncoupled Case of Microring Structure of Fig. 1 for Various Radius

Azimuthal mode index (Al)	R=1.2 $\mu$ m		Azimuthal mode index (Al)	R=2 $\mu$ m	
	Resonant wavelength [nm]	Q		Resonant wavelength [nm]	Q
6	1769	23	22	1690	34
7	1540	30	24	1547	43
8	1367	38	26	1408	54

(ordinary) and  $n_{E,LiNbO_3} = 2.1381$  (extraordinary), [62], while the dielectric constant of silver follows the Lorentz-Drude model.

Table 5 presents three resulting higher order eigenvalues of the uncoupled case of Fig. 1, which are compared with those of Fig. 2. The two geometries have similar geometrical characteristics, with the only differences being the ring radius ( $R_{Si} = 0.945 \mu\text{m}$ ,  $R_{LiNbO_3} = 1.2 \mu\text{m}$ ), the insertion of the silver ring at the bottom of the silica, which will play the role of the ground electrode at the electronic reconfiguration procedure, and the substitution of silicon layer ( $n_{Si} = 3.48$ ) with the a lithium niobate ( $LiNbO_3$ ,  $n_{ord.} \approx 2.21$ ) layer. The WGMs modes at their resonance exhibit an integer number of maxima defined by their azimuthal index (Al) and separated by half guided wavelength ( $\lambda_g = \lambda_0/n_{eff}$ ). Considering the same ring radius R, it should be:

$$\lambda\pi R = 2Al_{Si} \frac{\lambda_{g_{Si}}}{2} = 2Al_{LiNbO_3} \frac{\lambda_{g_{LiNbO_3}}}{2} \quad (15)$$

Since  $n_{eff,Si} > n_{eff,LiNbO_3}$ , this results to  $\lambda_{g,Si} < \lambda_{g,LiNbO_3}$  and thus,  $Al_{Si} < Al_{LiNbO_3}$ . It is known that for WGM the energy is better confined within the resonator as the Al increases. However, in our case, the ring radius of the silicon resonator is smaller than the  $LiNbO_3$  resonator. This geometrical scaling is responsible for the same level of resonant wavelengths of the modes of equal Al, as presented in Table 5. Nevertheless, the substitution of silicon layer with  $LiNbO_3$  yields a significant reduction of the quality factor as observed in Table 5, due to the lower index of refraction of  $LiNbO_3$  compared to silicon. This is the result of the higher energy leakage away from the ring, due to the lower field confinement, causing major reduction of the quality factor.

The significant deterioration of the quality factors explains the fact that the silicon-based resonators are dominant in photonic filtering structures, although their tuning capabilities are achieved through an inconvenient electrical control of temperature (electro-thermal). Besides that, silicon lacks second-order optical nonlinearity, limiting the application of silicon-based resonators at infrared wavelengths, [28], [61]. The large electro-optic coefficients, the resulting transparency from the ultraviolet to the infrared range and the wide intrinsic bandwidth are the principal reasons for the choice of  $LiNbO_3$ , although its use results in lower level quality factors and consequently in a reduced efficiency of the filtering structure. When the application allows, the diameter of the ring resonator is increased to attain the desired field confinement. Thus, if the microring radius increases, the resulting bending losses will be significantly reduced, boosting the quality factor at the same time. This is observed in the eigenvalues presented in Table 6, where the rings radius is increased, leading also to the desired azimuthal mode numbers increase, which explains why the  $LiNbO_3$  based ring resonators can yield tunable filtering structures supporting whispering gallery modes. Also, the increase of ring width will result in the further increase of the effective index and

TABLE 7

Comparison Between the Higher Order Eigenvalues of the Coupled Microring of Fig. 1 With Use of Only Classical  $abc_s$  and With the Implementation of Modified  $abc_s$

Mode No.	Azimuthal mode index (AI)	Only classical ABCs		Combined Classical ABCs and mABCs	
		Resonant wavelength [nm]	Q	Resonant wavelength [nm]	Q
1	-	1847	7	1859	10
2	6	1777	20	1777	21
3	6	1774	19	1773	19
4	-	1677	10	1684	13
5	-	1558	12	1568	14
6	7	1544	26	1543	26
7	7	1543	23	1539	26
8	-	1474	13	1478	18
9	8	1373	28	1379	29
10	8	1369	32	1369	32
11	-	1367	17	1365	24
12	-	1283	19	1286	29

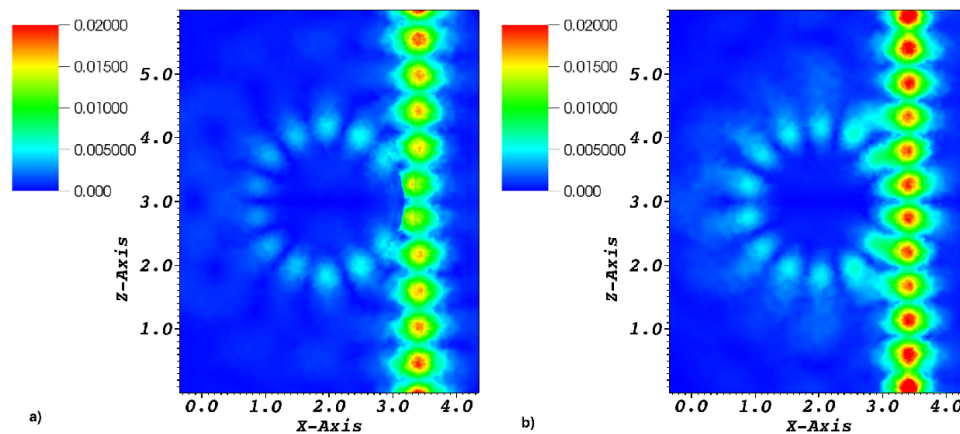


Fig. 7. Electric field distributions of the all-pass mode #5 (AI #7) of the geometry of Fig. 1 with the implementation of a) classical ABCs b) combined classical ABCs and mABCs at the waveguides ports.

a smaller wavelength corresponding to the increase of the quality factor due to the reduction of the energy leakage from the ring, [34].

**3.4.2 Analysis of the Coupled Ring-Bus Waveguide Resonator:** Concerning the case where the microring is side coupled to a hybrid plasmonic waveguide (HPW) bus (Fig. 1), the modified Absorbing Boundary Conditions (mABCs) are inevitable. These are thoroughly presented in Section 2 and must be enforced at the input and output ports of the HPW, while on the remaining open surfaces, the classical ABCs are still enforced. During the formulation of the problem, a 2D eigenvalue analysis at the input/output ports is needed to determine the dominant modes wave impedance. Implementing this 2D analysis with the aid of the commercial simulator COMSOL Multiphysics, [63], the wave impedances for the TE and TM modes are obtained at different resonant wavelengths. The resulting eigenvalues are derived and listed in Table 7. Observing the results, significant mismatches appear in the modes #1, #4, #5, #8, #11 and #12, which refer to the cases where the resonator operates as a perfect all-pass filter (with little or no energy circulation inside the ring). The resulting deviations mainly exist in the resonant wavelengths, and they have a minor affect on the quality factors.

To prove the necessity of waveguide termination at mABCs, Fig. 7 shows the field distribution for the mode with azimuthal index #7 (all-pass) both in the case when only classical ABCs and in the case when the combined classical ABCs and mABCs are enforced. It is evident that in the first case (Fig. 7a), there is much accumulation of energy at the input and output ports of the waveguide, which

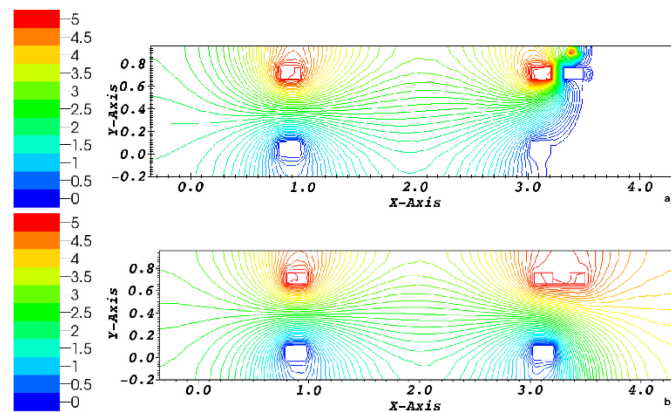


Fig. 8. Electric potential distributions at the horizontal Cut-4 of Fig. 1b for 5 volts application a) only in the upper silver ring layer b) in the upper silver layers of both ring and waveguide.

probably reveals the existence of reflectance due to mismatches. On the contrary, the existence of mABCs (Fig. 7b) eliminates this problem and thus there is no excessive energy at the ports than the other parts of the waveguide.

Concerning the structure depicted in Fig. 1, a DC voltage is applied in the first case only to the upper silver ring layer, while the bottom silver ring layer serves as the ground layer ( $V=0$  volts). In the second case the same DC voltage is also applied to the waveguides silver layer. After the application of DC voltage, an electric potential distribution between the silver layers is developed, which leads to the appearance of a static electric field distribution. Fig. 8 depicts the static electric potential distribution at the horizontal Cut-4 of Fig. 1b for the two different cases of applied voltage (5 volts). Note that in Fig. 8a the positive 5V DC electrode is connected only to the ring electrode, causing the nearby metal layer on top of HPW waveguide to be virtually grounded. This results in a highly unsymmetrical potential distribution of Fig. 8a with high gradient on the area around the bus waveguide, which is undesirable. In contrast, when the 5 V positive electrode is also connected to the HPW top metal, the symmetric potential distribution of Fig. 8b is obtained. This inhomogeneous nature of the developed potential justifies the necessity of a piecewise homogeneous optical permittivity tensor distribution in the electronically tunable case, rather than a constant mean value.

**3.4.3 Electronically Tunable  $\text{LiNbO}_3$  Ring Resonator:** Comparing the eigenvalues of the uncoupled and the coupled case of Fig. 1, as presented in Tables 5 and 7, a reduction of the quality factors are clearly evident as a result of the coupling between microring and bus waveguide, [64], whereas the resonant wavelength varies in each mode. To prove the validity of the results, Fig. 9 depicts the field distribution of both the uncoupled and the coupled case for mode #6 (AI #7) correspondingly.

Thus, having calculated the electric potential distribution with the generalized Laplace equation, as presented in section 2, the corresponding electric field distribution is computed. The maximum value of electric field in our study is between the corresponding ones used in other published works, [27]–[28]. In turn, the altered index of refraction tensor of  $\text{LiNbO}_3$  at THz or photonic frequencies is calculated as piecewise constant distribution utilizing the closed form expressions of [29].

Fig. 10 depicts a 3D representation of the ordinary index of refraction at Cut-4 of Fig. 1b when a 5V voltage is applied only to the upper silver ring layer. This image is misleading in characterizing the  $\text{LiNbO}_3$ s ordinary and extraordinary indexes of refraction by a constant mean value. However, this presentation totally delineates the occurring variations due to the inhomogeneity of the developed electric field distribution. Indicatively, it is common knowledge that a very small difference in the index of refraction may confine the optical wave (as in silica optical fibers, for example). In order to reveal the level of the resulting deviations of  $\text{LiNbO}_3$ s ordinary and extraordinary indexes of refraction when a DC voltage is applied in the upper ring layer, some of their distributions for different

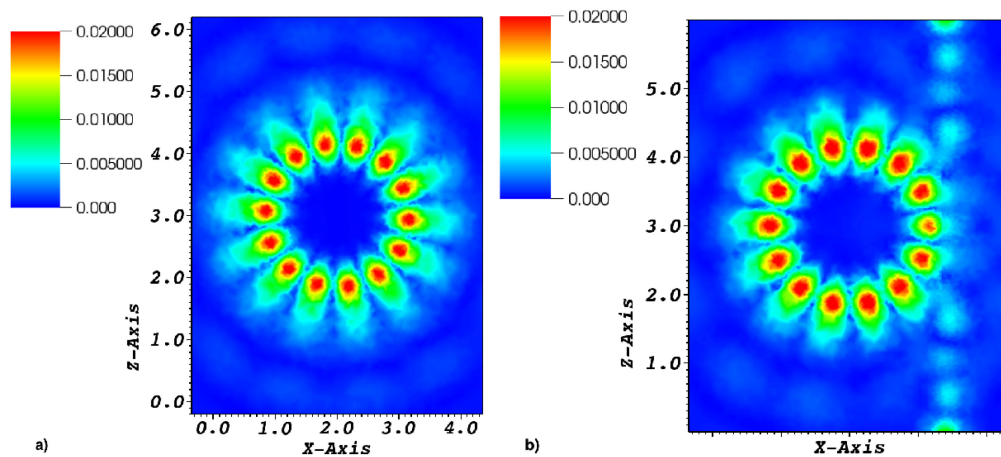


Fig. 9. Electric field distributions of a) the uncoupled and b) coupled case of the azimuthal index #7.

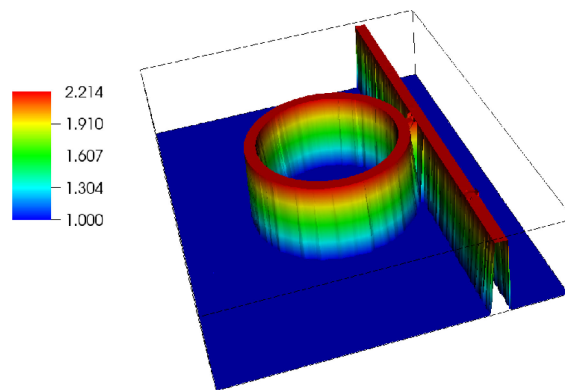


Fig. 10. 3D representation of ordinary index of refraction distribution at the Cut-4 of Fig. 1b for 5 V applied voltage.

cuts (Fig. 1b) are presented. In particular, Fig. 11–13 show the distributions of ordinary index of refraction for different areas of  $LiNbO_3$  and for various applied DC voltages for both the case when a DC voltage is applied only on the upper silver ring layer (continuous line) and the case when the same DC voltage is also applied to the waveguides silver layer (dotted line). The distributions of extraordinary index of refraction have a similar form. Concerning the observed variations inside the  $LiNbO_3$  layer, these reach the order of  $10^{-4}$ , even for the same level of applied DC voltage. As mentioned above the refractive index profile of optical fiber has alterations of the order of  $10^{-2}$  in order to accomplish an almost perfect confinement of light inside the core section. Thus, consideration of the aforementioned variations is crucial for the correct solution of the eigenproblem. This is accomplished in our algorithm by usage of a piecewise homogeneous permittivity tensor distribution for  $LiNbO_3$ . Besides that, Figs. 11, 12 and 13 reveal the importance of the DC positive electrodes connection to the HPW top metal layer in ensuring a relatively homogeneous potential distribution and thus a more uniform optical index of refraction.

Table 8 lists the eigenvalues of the mode with azimuthal index #7 for the geometry of Fig. 1, when a variety of external applied DC voltages for both the case where only the top silver ring layer is excited and the case when the DC voltage is also enforced in the silver layer of waveguide. The shifts of the resonant wavelength caused by changes of the effective index of the resonant mode



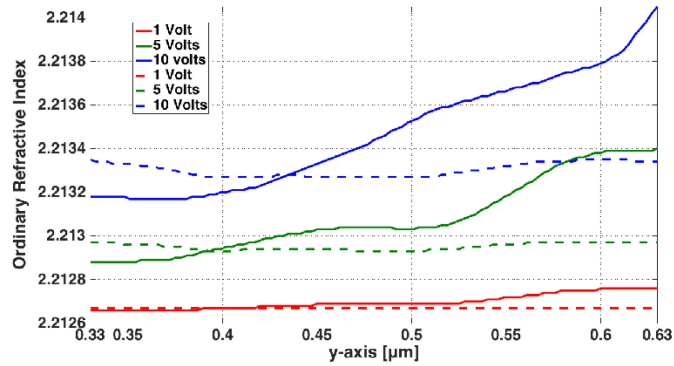


Fig. 11. Ordinary index of refraction distribution at the vertical Cut-1 near the feeding waveguide of Fig. 1b for a variety of applying voltages (continuum line as in Fig. 8a, dotted line as in Fig. 8b).

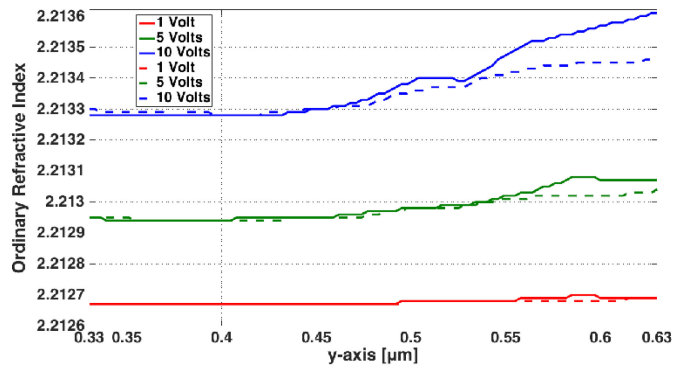


Fig. 12. Ordinary index of refraction distribution at the vertical Cut-2 near the feeding waveguide of Fig. 1b for a variety of applying voltages (continuum line as in Fig. 8a, dotted line as in Fig. 8b).

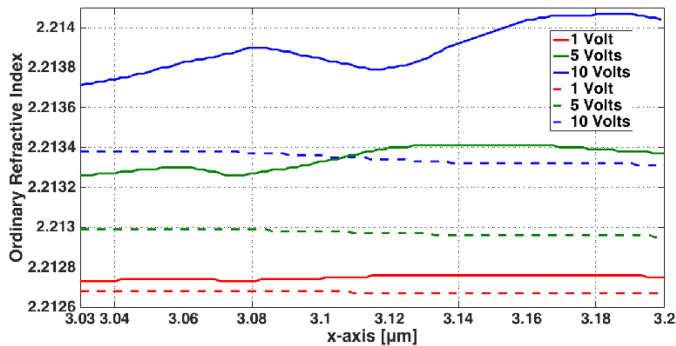


Fig. 13. Ordinary index of refraction distribution at the vertical Cut-3 near the feeding waveguide of Fig. 1b for a variety of applying voltages (continuum line as in Fig. 8a, dotted line as in Fig. 8b).

$n_{eff}$  track the following equation reasonable well [32]:

$$\Delta\lambda_{res} = \frac{\Delta n_{eff} L}{m}, m = 1, 2, \dots \quad (16)$$

where  $L = 2\pi R$  is the round trip length ( $R$ : mean ring radius) and  $m$  is the order of the resonant mode. The largest observed alterations of resonant wavelength in the case of the DC voltage being applied only to the upper silver layer of the ring are expected due to the greater inhomogeneity of

TABLE 8  
Eigenvalues for the Mode With Azimuthal Index #7 for the Structure of Fig. 1 Applying Different dc Voltage Levels

Voltage Applied [Volts]	Silver Ring Layer Excitation		Silver Ring and Waveguide Layers Excitation	
	Resonant wavelength [nm]	Q	Resonant wavelength [nm]	Q
-	1543	26	1543	26
1	1545.45	29.07	1544.05	30.65
5	1545.79	29.46	1544.16	30.79
10	1546	29.97	1544.4	30.83

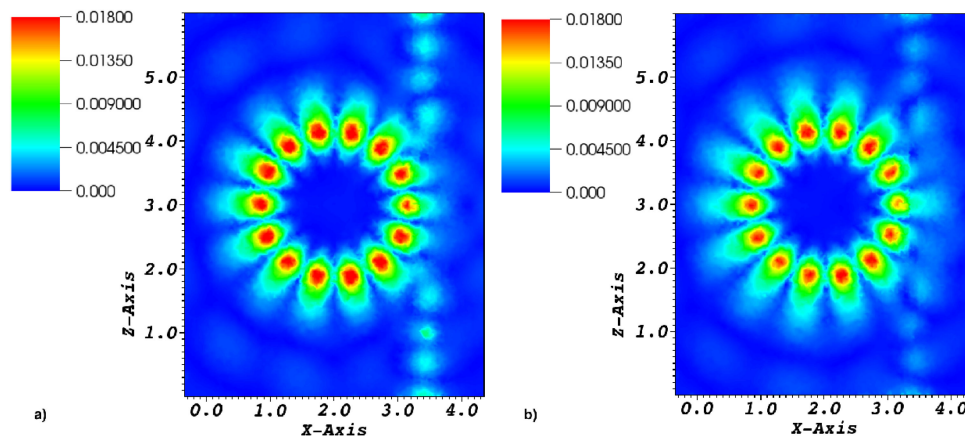


Fig. 14. Electric field distributions of the mode with azimuthal index #7 for the case of a) 5V and b) 10V applied voltage.

TABLE 9  
Eigenvalues for the Mode With Azimuthal Index #7 for the Structure of Fig. 1 Applying Different dc Voltage Levels and Utilizing Both a Constant Mean Value and a Piecewise Homogeneous Distribution for the  $LiNbO_3$  Refractive Index

Voltage Applied [Volts]	Constant Mean Value		Silver Ring Layer Excitation	
	Resonant wavelength nm	Q	Resonant wavelength nm	Q
-	1543	26	1543	26
1	1543.2	26.64	1545.45	29.07
5	1543.5	26.67	1545.79	29.46
10	1543.8	26.71	1546	29.97

the resulting voltage distribution in the geometry (Fig. 8), which is also responsible for the larger variations of indexes of refraction (Fig. 11–13).

The form of the resulting field distributions of the modes remains unaffected for the different levels of applied DC voltages, as depicted in Fig. 14 for the cases when 5 V and 10 V are applied only to the upper silver ring layer. The same situation occurs when the waveguides silver layer is also excited. Concerning the quality factor, it has a minor increase after the application of a DC voltage. This increase is probably the result of the implementation of the increased index of refraction for the piecewise homogeneous dielectric permittivity tensor distribution for  $LiNbO_3$  and thus a better confinement of light, which does not exist in the initial condition (zero applied voltage), where a constant value for the dielectric permittivity is considered.

The necessity of utilizing a piecewise constant distribution for  $LiNbO_3$ s index of refraction, when an external DC voltage is applied, is evident from the distributions of Figs. 11–13. To further show the significant role of this approach, Table 9 lists the eigenvalues of the studied geometry of Fig. 1 when a constant mean value is used for the  $LiNbO_3$ s refractive index for the different levels of the applied DC voltage in the upper silver ring layer. The resultant deviations of these eigenvalues

compared with the corresponding ones of Table 8 are significant, which reflect on the importance of correct characterization of the altered index of refraction.

#### 4. Conclusions

A numerical eigenanalysis tool for the study of tunable terahertz and photonic structures has been established. For the treatment of metallic parts in the THz and photonic spectrum, the Lorentz-Drude model has been employed. The important frequency variation of the metal complex dielectric constant is accounted for by employing an iterative solution of the resulting non-linear eigenproblem. The analysis has been focused on microring-based resonators. The large electro-optic coefficients that  $LiNbO_3$  exhibits are exploited for the enforcement of electrical tunability. The novelty in our approach stems from the consideration of the altered refractive index of  $LiNbO_3$  as a piecewise constant distribution, a more accurate approach than the constant mean value considered so far. Furthermore, a tree-cotree technique has been utilized in the formulation of the eigenvalue problem for the removal of DC and imaginary spurious modes.

#### References

- [1] A. J. Seeds and K. J. Williams, "Microwave photonics," *J. Lightwave Technol.*, vol. 24, pp. 4628–4641, 2006.
- [2] S. Iezekiel, ed., *Microwave Photonics: Device and Applications*. Hoboken, NJ, USA: Wiley, 2009.
- [3] T. Berceli and P. Herczfeld, "Microwave photonics historical perspective," *IEEE Trans. Microw. Theory Techn.*, vol. 58, no. 11, pp. 2992–3000, Nov. 2010.
- [4] T. R. Clark and R. Waterhouse, "Photonics for RF front ends," *IEEE Microw. Mag.*, vol. 12, no. 3, pp. 87–95, May 2011.
- [5] D. K. Gramotnev and S. I. Bozhevolnyi, "Plasmonics beyond the diffraction limit," *Nature Photon.*, vol. 4, pp. 83–91, 2010.
- [6] C. Zekios, P. Allilomes, M. Chryssomallis, P. Gkonis, I. Venieris, and G. Kyriacou, "A finite element eigenanalysis of electrically large THz and photonic structures," in *Proc. Eur. Conf. Antennas Propag.*, 2014, pp. 3331–3334.
- [7] A. Al and N. Engheta, "Theory modeling and features of optical nanoantennas," *IEEE Trans. Antennas Propag.*, vol. 61, no. 4, pp. 1508–1517, Apr. 2013.
- [8] Z. Ma and G. A. E. Vandenbosch, "Systematic full-wave characterization of real-metal nano dipole antennas," *IEEE Trans. Antennas Propag.*, vol. 61, no. 10, pp. 4990–4999, Oct. 2013.
- [9] C. L. Zekios, P. C. Allilomes, and G. A. Kyriacou, "DC and imaginary spurious modes suppression for both unbounded and lossy structures," *IEEE Trans. Microw. Theory Techn.*, vol. 63, no. 7, pp. 2082–2093, May 2015.
- [10] C. L. Zekios, P. C. Allilomes, M. T. Chryssomallis, and G. A. Kyriacou, "Finite element based eigenanalysis for the study of electrically large lossy cavities and reverberation chambers," *Prog. Electromagn. Res. B*, vol. 61, pp. 269–296, 2014.
- [11] C. L. Zekios, P. C. Allilomes, and G. A. Kyriacou, "On the evaluation of eigenmodes quality factor of large complex cavities based on a PEC linear finite element formulation," *Electron. Lett.*, vol. 48, no. 22, pp. 1399–1401, Oct. 2012.
- [12] G. A. E. Vandenbosch, V. Volskiy, N. Verellen, and V. V. Moshchalkov, "On the use of the method of moments in plasmonic applications," *Radio Sci.*, vol. 46, 2011, Art. no. RS0E02.
- [13] C. Zekios, P. Allilomes, and G. Kyriacou, "Eigenanalysis of photonic structures based on finite element with efficient suppression of spurious modes," in *Proc. IEEE Int. Conf. Comput. Electromag.*, Hong Kong, Feb. 2015, pp. 129–131.
- [14] E. Le Ru and P. Etchegoin, *Principles of Surface-enhanced Raman Spectroscopy and Related Plasmonic Effects*, Oxford, U.K.: Elsevier, 2008.
- [15] A. D. Raki, A. B. Djurii, J. M. Elazar, and M. L. Majewski, "Optical properties of metallic films for vertical-cavity optoelectronic devices," *Appl. Opt.*, vol. 37, pp. 5271–5283, 1998.
- [16] S. A. Maier, *Plasmonics: Fundamentals and Applications*. Berlin, Germany: Springer, 2007, pp. 65–87.
- [17] W. L. Barnes, "Surface plasmon polariton length scales: A route to sub-wavelength optics," *J. Opt. A*, vol. 8, pp. S87–S93, 2006.
- [18] R. Qiang, R. L. Chen, and J. Chen, "Modeling electrical properties of gold films at infrared frequency using FDTD method," *Int. J. Infrared Millimeter Waves*, vol. 25, no. 8, pp. 1263–1270, 2004.
- [19] I. Chremmos, O. Schwelb, and N. Uzunoglu, *Photonic Microresonator Research and Applications*. New York, NY, USA: Springer, 2010.
- [20] X. Zheng *et al.*, "Implementation of the natural mode analysis for nanotopologies using a volumetric method of moments (V-MoM) algorithm," *IEEE Photon. J.*, vol. 6, no. 4, Aug. 2014, Art. no. 4801413.
- [21] L. Novotny and B. Hecht, *Principles of Nano-Optics*. Cambridge, U.K.: Cambridge Univ. Press, 2006.
- [22] B. E. A. Saleh and M. C. Teich, *Fundamental of Photonics*. Hoboken, NJ, USA: Wiley, 1991.
- [23] D. A. Ketzaki, O. Tsilipakos, T. V. Yioultsis, and E. E. Kriezis, "Electromagnetically induced transparency with hybrid silicon-plasmonic traveling-wave resonators," *J. Appl. Phys.*, vol. 114, 2013, Art. no. 113107.
- [24] E. Wooten *et al.*, "A review of lithium niobate modulators for fiber-optic communications systems," *IEEE J. Sel. Topics Quantum Electron.*, vol. 6, no. 1, pp. 69–82, Jan./Feb. 2000.
- [25] H. Lu *et al.*, "Optical and RF characterization of a lithium niobate photonic crystal modulator," *IEEE Photon. Technol. Lett.*, vol. 26, no. 13, pp. 1332–1335, Jul. 2014.

- [26] S. Zhou *et al.*, "Add-drop filter based on wavelength-dependent light interlink between lithium-niobate microwave guide chip and microfiber knot ring," *Crystals*, vol. 6, no. 6, p. 67, 2016, doi: [10.3390/cryst6060067](https://doi.org/10.3390/cryst6060067).
- [27] L. Chen, M. G. Wood, and R. M. Reano, "12.5 pm/V hybrid silicon and lithium niobate optical microring resonator with integrated electrodes," *Opt. Express*, vol. 21, pp. 27003–27010, 2013.
- [28] A. Guarino, G. Poberaj, D. Rezzonico, R. DeglInnocenti, and P. Gunter, "Electrooptically tunable microring resonators in lithium niobate," *Nature Photon.*, vol. 1, pp. 407–410, Jul. 2007.
- [29] E. N. Glytsis, T. K. Gaylord, and M. G. Moharam, "Electric field, permittivity, and strain distributions induced by interdigitated electrodes on electrooptic waveguides," *J. Lightw. Technol.*, vol. LT-5, no. 5, pp. 668–683, May 1987.
- [30] M. Luennemann, U. Hartwig, G. Panotopoulos, and K. Buse, "Electrooptic properties of lithium niobate crystals for extremely high external electric fields," *Appl. Phys. B*, vol. 76, pp. 403–406, 2003, doi: [10.1007/s00340-003-1123-9](https://doi.org/10.1007/s00340-003-1123-9).
- [31] K. D. Paschaloudis, C. L. Zekios, P. C. Allilomes, and G. A. Kyriacou, "An eigenanalysis study of photonic-THz tunable ring resonators and phase shifters employing finite element method," in *Proc. 36th ES Antenna Workshop Antenna RF Syst. Space Sci.*, Noordwijk, The Netherlands, Oct. 2015, pp. 1–7.
- [32] W. Bogaerts *et al.*, "Silicon microring resonators," *Laser Photon. Rev.*, vol. 6, no. 1, pp. 47–73, 2012, doi: [10.1002/lpor.201100017](https://doi.org/10.1002/lpor.201100017).
- [33] T. Barwicz *et al.*, "Fabrication of add-drop filters based on frequency-matched microring resonators," *J. Lightw. Technol.*, vol. 24, no. 5, pp. 2207–2218, May 2006.
- [34] L. Chrostowski and M. Hochberg, *Silicon Photonics Design: From Devices to Systems*. Cambridge, U.K.: Cambridge Univ. Press, 2015, doi: [10.1017/CBO9781316084168](https://doi.org/10.1017/CBO9781316084168)
- [35] A. Delage *et al.*, "Wavelength-dependent model of a ring resonator sensor excited by a directional coupler," *J. Lightw. Technol.*, vol. 27, no. 9, pp. 1172–1180, May 2009.
- [36] P. Rabiei, W.H. Steier, C. Zhang, and L. R. Dalton, "Polymer micro-ring filters and modulators," *J. Lightw. Technol.*, vol. 20, no. 11, pp. 1968–1975, Nov. 2002.
- [37] M. Forst *et al.*, "High-speed all-optical switching in ion-implanted silicon- on-insulator microring resonators," *Opt. Lett.*, vol. 32, pp. 2046–2048, 2007.
- [38] V. Van, T. A. Ibrahim, P. P. Absil, F. G. Johnson, R. Grover, and P.-T. Ho, "Optical signal processing using nonlinear semiconductor microring resonators," *IEEE J. Sel. Topics Quantum Electron.*, vol. 8, no. 3, pp. 705–713, May/June 2002.
- [39] J. B. Khurgin, "Optical buffers based on slow light in electromagnetically induced transparent media and coupled resonator structures: comparative analysis," *J. Opt. Soc. Amer. B*, vol. 22, pp. 1062–1074, 2005.
- [40] B. E. Little *et al.*, "Very high-order microring resonator filters for WDM applications," *IEEE Photon. Technol. Lett.*, vol. 16, no. 10, pp. 2263–2265, Oct. 2004.
- [41] T. Barwicz, M. A. Popovic, M. R. Watts, P. T. Rakich, E. P. Ippen, and H. I. Smith, "Fabrication of add-drop filters based on frequency-matched microring resonators," *J. Lightw. Technol.*, vol. 24, no. 5, pp. 2207–2218, May 2006.
- [42] J. V. Hryniewicz, P. P. Absil, B. E. Little, R. A. Wilson, and P.-T. Ho, "Higher order filter response in coupled microring resonators," *IEEE Photon. Technol. Lett.*, vol. 12, no. 3, pp. 320–322, Mar. 2000.
- [43] M. Wu, Z. Han, and V. Van, "Conductor-gap-silicon plasmonic waveguides and passive components at subwavelength scale," *Opt. Express*, vol. 18, pp. 11728–11736, 2010.
- [44] R. F. Oulton *et al.*, "A hybrid plasmonic waveguide for subwavelength confinement and long-range propagation," *Nature Photon.*, vol. 2, pp. 496–500, 2008.
- [45] Y. Zhu and A. C. Cangellaris, *Multigrid Finite Element Methods for Electromagnetic Field Modeling*. Piscataway, NJ, USA: IEEE Press, 2006.
- [46] P. B. Johnson and R. W. Christy, "Optical constants of the noble metals," *Phys. Rev. B*, vol. 6, no. 12, pp. 4370–4379, 1972.
- [47] J. L. Volakis, A. Chatterjee, and L. C. Kempel, *Finite Element Method Electromagnetics: Antennas, Microwave Circuits and Scattering Applications*. New York, NY, USA: Wiley, 1998.
- [48] J. -S. Wang and R. Mittra, "Finite element analysis of MMIC structures and electronic packages using absorbing boundary conditions," *IEEE Trans. Microw. Theory Techn.*, vol. 42, no. 3, pp. 441–449, Mar. 1994.
- [49] A. C. Polycarpou, M. R. Lyons, and C. A. Balanis, "Finite element analysis of MMIC waveguide structures with anisotropic substrates," *IEEE Trans. Microw. Theory Techn.*, vol. 44, pp. 1650–1663, Oct. 1996.
- [50] O. Tsilipakos, E. E. Kriezis, and T. V. Yioultis, "Boundary condition for the efficient excitation and absorption of hybrid waveguide modes in finite element formulations," *Microw. Opt. Technol. Lett.*, vol. 53, 2011, Art. no. 2626.
- [51] H. Guo, "3-dimensional eigenmodal analysis of electromagnetic structures," ETH Zurich, Zurich, Switzerland, Tech. Rep. 20947, 2012.
- [52] N. V. Venkatarayalu and J. F. Lee, "Removal of spurious DC modes in edge element solutions for modeling three-dimensional resonators," *IEEE Trans. Microw. Theory Techn.*, vol. 54, no. 7, pp. 3019–3025, Jul. 2006.
- [53] C. Zekios, "Electromagnetic simulation and eigen-analysis of three dimensional radiating structures based on the finite element method," Ph.D. dissertation, Democritus Univ. Thrace, Xanthi, Greece, 2015.
- [54] R. F. Sviercoski, C. L. Winter, and A. C. Warrick, "Analytical approximation for the generalized laplace equation with step function coefficient," *SIAM J. Appl. Math.*, vol. 68, no. 5, pp. 1268–1281, 2008.
- [55] SALOME: *Open Source Integration Platform for Numerical Simulation*, Std. [Online]. Available: <http://www.salome-platform.org/>
- [56] A. Logg, K. A. Mardal, and G. Wells, *Automated Solution of Differential Equations by the Finite Element Method*. Berlin, Germany: Springer, 2013.
- [57] M. A. Ordal, R. J. Bell, R. W. Alexander, L. L. Long, and M. R. Querry, "Optical properties of fourteen metals in the infrared and far infrared: Al, Co, Cu, Au, Fe, Pb, Mo, Ni, Pd, Pt, Ag, Ti, V, and W," *Appl. Opt.*, vol. 24, pp. 4493–4499, 1985.
- [58] H. U. Yang, J. D'Archangel, M. L. Sundheimer, E. Tucker, G. D. Boreman, and M. B. Raschke, "Optical dielectric function of silver," *Phys. Rev. B*, vol. 91, 2015, Art. no. 235137.

- [59] H. E. Bennett and J. M. Bennett, *Optical Properties and Electronic Structure of Metals and Alloys*, F. Abeles, ed., New York, NY, USA; Wiley, 1966.
- [60] P. Winsemius, H. Lengkeek, and F. Van Kampen, "Structure dependence of the optical properties of Cu, Ag and Au," *Physica B+C*, vol. 79, no. 6, pp. 529–546, 1975.
- [61] P. Rabiei, J. Ma, S. Khan, J. Chiles, and S. Fathpour, "Heterogeneous lithium niobate photonics on silicon substrates," *Opt. Express*, vol. 21, pp. 25573–25581, 2013.
- [62] D. F. Nelson and R. M. Mikulyak, "Refractive indices of congruently melting lithium niobate," *J. Appl. Phys.*, 1974, vol. 45, no. 8, pp. 3688–3689.
- [63] COMSOL, *Product Suite of Multiphysics Software*. [Online]. Available: <https://www.comsol.com/>
- [64] M. A. Popovi, C. Manolatu, and M. R. Watts, "Coupling-induced resonance frequency shifts in coupled dielectric multi-cavity filters," *Opt. Express*, vol. 14, pp. 1208–1222, 2006.